

# Structures and Electrochemical Hydrogen Storage Properties of the As-Spun RE-Mg-Ni-Co-Al-Based AB<sub>2</sub>-Type Alloys Applied to Ni-MH Battery



YANGHUAN ZHANG, ZEMING YUAN, HONGWEI SHANG, YAQIN LI, YAN QI, and DONGLIANG ZHAO

In this paper, the La<sub>0.8-x</sub>Ce<sub>0.2</sub>Y<sub>x</sub>MgNi<sub>3.5</sub>Co<sub>0.4</sub>Al<sub>0.1</sub> ( $x = 0, 0.05, 0.1, 0.15, 0.2$ ) alloys were synthesized *via* smelting and melt spinning. The effect of Y content on the structure and electrochemical hydrogen storage characteristics of the as-cast and spun alloys was investigated. The identifications of XRD and SEM demonstrate that the experimental alloys possess a major phase LaMgNi<sub>4</sub> and a minor phase LaNi<sub>5</sub>. The variation of Y content results in an obvious transformation of the phase abundance rather than phase composition in the alloys, namely LaMgNi<sub>4</sub> phase increases while LaNi<sub>5</sub> phase decreases with Y content growing. Furthermore, the replacement of Y for La causes the lattice constants and cell volume to clearly decrease and markedly refines the alloy grains. The electrochemical tests reveal that these alloys can obtain the maximum values of discharge capacity at the first cycling without any activation needed. With Y content growing, the discharge capacity of the alloys obviously declines, but its cycle stability remarkably improves. Moreover, the electrochemical dynamics of the alloys, involving the high-rate discharge ability, hydrogen diffusion coefficient ( $D$ ), limiting current density ( $I_L$ ), and charge transfer rate, initially augment and then decrease with rising Y content.

DOI: 10.1007/s11661-017-4052-7

© The Minerals, Metals & Materials Society and ASM International 2017

## I. INTRODUCTION

THE end of the Stone Age is not because of the depletion of the stone. Likewise, the end of the fossil fuel era does not need to wait until it dries up. In other words, human beings cannot be forced to abandon the car due to the exhaustion of fossil fuels; instead, mankind is very likely to initiatively give up fossil fuels in the case of the great development of the automobile. The excessive consumption of limited fossil fuels causes a series of environmental problems. Especially, the dramatic growth of the global warming rate and air pollution index has attracted widespread international attention and concerns. Also, it was reported that approximately 25 pct of world total energy was consumed by transport<sup>[1]</sup> and globally above 23 pct CO<sub>2</sub> emissions from vehicular waste gases *via* the combustion of fossil fuels.<sup>[2,3]</sup> Hence, a widespread application of electric vehicle (EV) and hybrid electric vehicle (HEV) is considered to be a potential approach to reduce both

carbon dioxide emissions and fossil energy consumption. Some hydrogen storage materials are considered to be candidates as the negative electrode of Ni-MH batteries, especially the rare earth (RE)-based AB<sub>2</sub> and AB<sub>5</sub>-type alloys which have achieved a large-scale commercial application, but none of them is satisfactory because of some of their inherent shortcomings, including the difficulty of being activated for AB<sub>2</sub> alloy and the relatively low specific capacity for AB<sub>5</sub> alloy. Considering comprehensive electrochemical property, RE-Mg-Ni-based AB<sub>2</sub>-type and A<sub>2</sub>B<sub>7</sub>-type alloys were viewed as the most attractive and potential candidates for the negative electrode<sup>[4,5]</sup> due to their lower production cost and reach to 380 to 410 mAh/g of discharge capacities, as claimed by Kohno *et al.*<sup>[6]</sup> and Kadir *et al.*<sup>[7]</sup> Wang *et al.*<sup>[8]</sup> provided LaMgNi<sub>4</sub> alloys synthesized by mechanical milling and measured its maximum discharge capacity which was about 400 mAh/g. Although extensive studies have been recently performed to achieve the goal of commercial application as supported by Liu *et al.*,<sup>[9,10]</sup> however, those attempts were thwarted by the poor cycle stability of those alloys. Consequently, researchers in this area still face a major challenge: finding a new type hydrogen storage alloy that can be applied in practical negative electrode.

Microstructure refining and alloying are verified to be effective methods for improving the hydrogen storage characteristics of La-Mg-Ni-based AB<sub>2</sub>-type alloy.<sup>[11,12]</sup> Particularly, the replacements of La by RE (Ce, Nd, Pr, and Sm) and Ni by transition elements (Co, Mn, Al, and Cu) can markedly improve the electrochemical cycle stability of the alloys.<sup>[13-15]</sup> Moreover, our previous

---

YANGHUAN ZHANG is with the Elected State Key Laboratory, Inner Mongolia University of Science and Technology, 7 Aerding Avenue, Baotou 014010, People's Republic of China, and also with the Department of Functional Material Research, Central Iron and Steel Research Institute, 76 Xueyuannan Road, Beijing 100081, People's Republic of China. Contact e-mail: zhangyh59@sina.com ZEMING YUAN, HONGWEI SHANG, YAQIN LI, YAN QI and DONGLIANG ZHAO are with the Department of Functional Material Research, Central Iron and Steel Research Institute, People's Republic of China.

Manuscript submitted November 10, 2016.

Article published online March 10, 2017

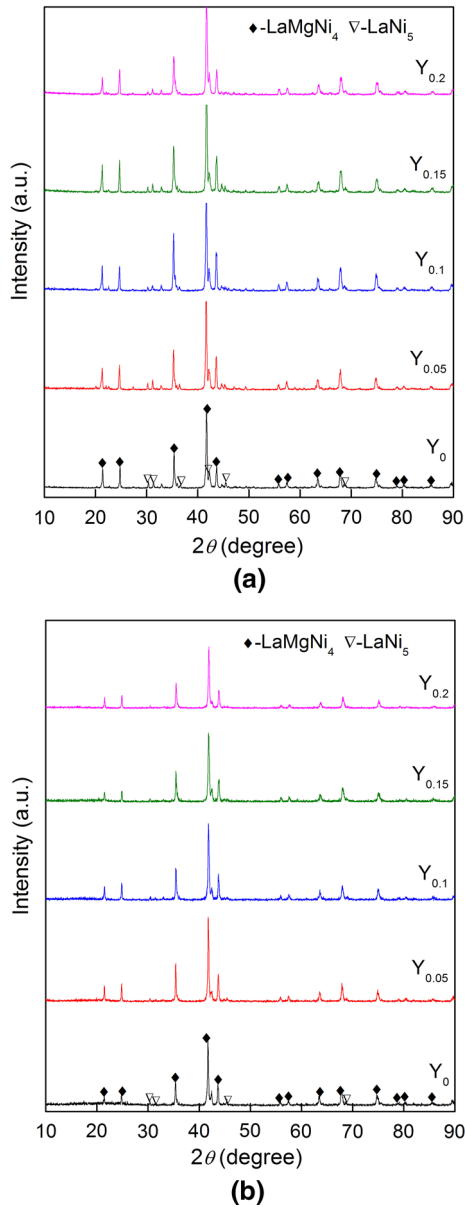


Fig. 1—XRD profiles of the as-cast and spun  $\text{La}_{0.8-x}\text{Ce}_{0.2}\text{Y}_x\text{MgNi}_{3.5}\text{Co}_{0.4}\text{Al}_{0.1}$  ( $x = 0$  to  $0.2$ ) alloys: (a) As-cast and (b) As-spun (10 m/s).

works revealed that melt spinning technology can greatly refine the structure of La-Mg-Ni system  $\text{A}_2\text{B}_7$ -type alloys and dramatically improve their electrochemical cycle stability.<sup>[16,17]</sup> Hence, we expect to combine the optimal Y substitution amount with appropriate melt spinning time to obtain an alloy which possesses higher discharge capacity as well as excellent electrochemical cycle stability.

It was confirmed that adding rare earth elements Y and Ce can significantly enhance the corrosion resistance of an electrode material, accordingly ameliorate its electrochemical properties, especially the cycle stability.<sup>[18,19]</sup> In the present work, Ce and Y were adopted to partially substitute La, and melt spinning technology was applied to synthesize  $\text{La}_{0.8-x}\text{Ce}_{0.2}\text{Y}_x\text{MgNi}_{3.5}\text{Co}_{0.4}\text{Al}_{0.1}$  ( $x = 0$  to

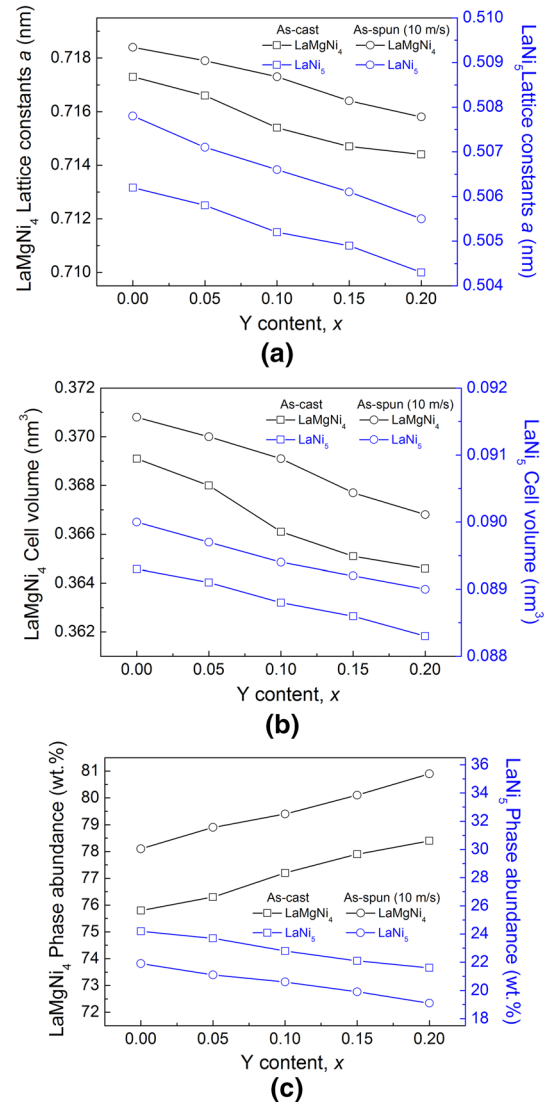


Fig. 2—Lattice parameters and phase abundances of  $\text{LaMgNi}_4$  and  $\text{LaNi}_5$  phases in the as-cast and spun (10 m/s)  $\text{La}_{0.8-x}\text{Ce}_{0.2}\text{Y}_x\text{MgNi}_{3.5}\text{Co}_{0.4}\text{Al}_{0.1}$  ( $x = 0$  to  $0.2$ ) alloys: (a) lattice constants  $a$ , (b) cell volume, and (c) phase abundances.

$0.2$ ) alloys. Subsequently, the influences of Y substitution amount on the microstructure and electrochemical hydrogen storage performances of the alloys have been studied at great length.

## II. EXPERIMENTAL

For convenience, those experimental alloys with nominal compositions of  $\text{La}_{0.8-x}\text{Ce}_{0.2}\text{Y}_x\text{MgNi}_{3.5}\text{Co}_{0.4}\text{Al}_{0.1}$  ( $x = 0, 0.05, 0.1, 0.15, 0.2$ ) were expressed with Y element content as  $\text{Y}_0, \text{Y}_{0.05}, \text{Y}_{0.1}, \text{Y}_{0.15}$ , and  $\text{Y}_{0.2}$ , respectively. The as-cast alloys were fabricated based on the vacuum-inducing smelting method. Owing to the large difference between Mg with other alloy elements (Mg is easy to evaporate because of its low melting point. Helium can effectively prevent Mg from

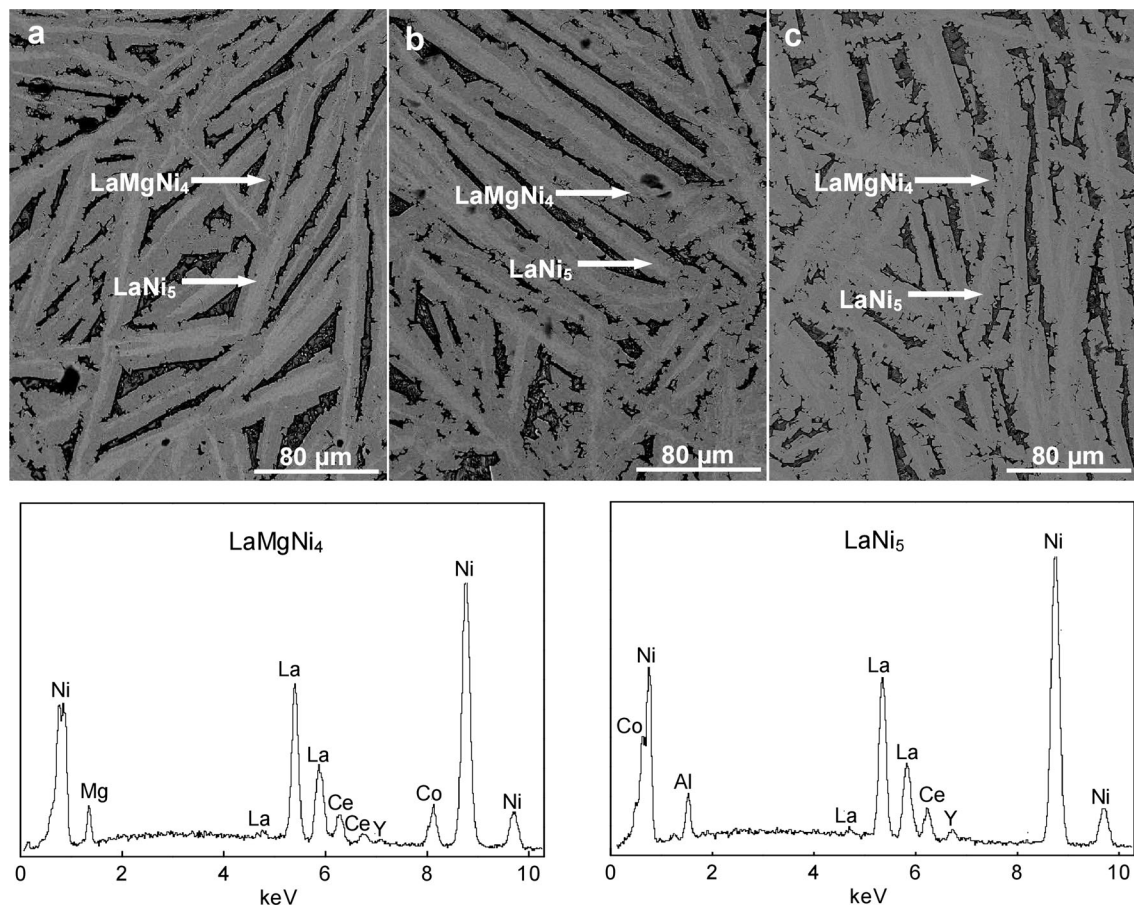


Fig. 3—SEM images together with typical EDS spectra of the as-cast alloys: (a)  $Y_0$  alloy, (b)  $Y_{0.1}$  alloy, (c)  $Y_{0.2}$  alloy.

volatilizing, but the mechanism remains unclear.), helium is filled into furnace about 0.04 MPa for avoiding the volatilization of Mg during smelting operation. Partial alloys were chosen to be re-melted and spun by melt spinning using a copper single roller. The linear velocity of the copper roller is regarded as the spinning rate as it is too hard to test the quenching rate of the alloys during spinning. In this work, the rates were set to be 2, 6, 10, and 15 m/s, respectively.

X-ray diffractometer (XRD) whose model is *D/max/2400* was used to research the phase composition and contents of the experimental alloys; the laboratorial parameters were set as follows: 160 mA, 40 kV, and 10 deg/minute. Scanning electron microscope (SEM) whose model is Philips Quanta 400 was utilized to observe the morphologies of the alloys, and the equipped energy-dispersive spectrometer (EDS) was used to determine the real chemical composition. The average grain size was determined using the line-intercept technique on five micrographs for each sample.

The alloy powder (0.20 g) was shaken with four times its weight of carbonyl nickel powder in a flask and subsequently cold pressed into  $\Phi 15$  mm round electrode pellet at 35 MPa. A metal hydride electrode acting as a working electrode, a sintered  $\text{Ni}(\text{OH})_2/\text{NiOOH}$  counter

electrode acting as a positive electrode, and a Hg/HgO reference electrode together constitute a tri-electrode open cell which was infused with 6 mol/L KOH electrolyte. It was used to measure the kinetics in electrochemical cycle. The voltage between the metal hydride electrode and Hg/HgO reference electrode was measured and selected as the discharge voltage. In each cycle, the alloy electrode was initially charged, after 15-minute intervals, and subsequently discharged until the voltage was down to  $-500$  mV at a certain current density.

An electrochemical workstation whose model is PARSTAT 2273 was used to measure the electrochemical impedance spectra (EIS) and the potentiodynamic polarization curves at 303 K (30 °C). The parameters of EIS tests were set to be that the frequency ranged from 10 kHz to 5 mHz, amplitude of signal was 5 mV, and number of points per decade of frequencies was 60. The EIS was tested at the state of 50 pct depth of discharge (DOD). With 5 mV/s scanning rate, the potentiodynamic polarization curves were tested in the potential range of  $-1.2$  to  $+1.0$  V (vs Hg/HgO). At last, the potentiostatic discharge of laboratorial electrodes in fully charged stage was measured using CorrWare electrochemistry corrosion software at 500 mV potential for 5000 seconds.

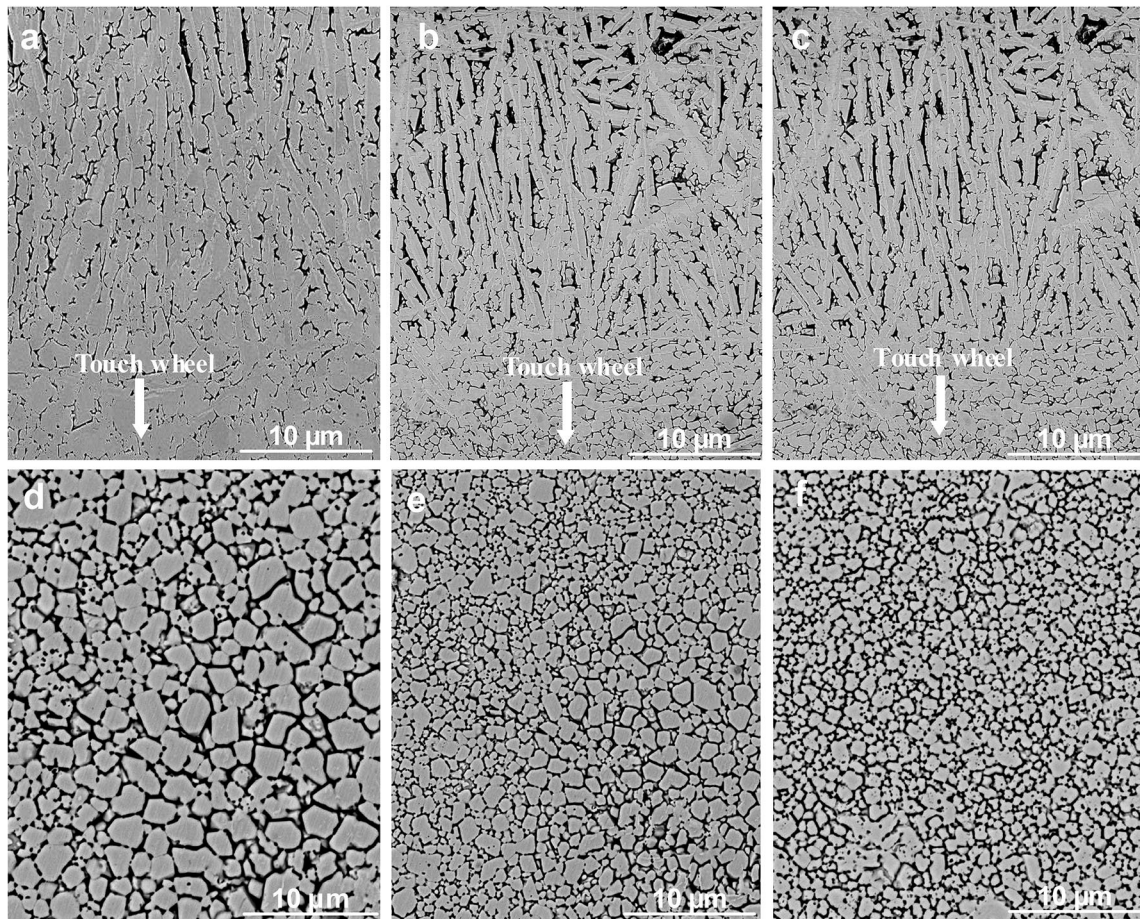


Fig. 4—SEM images of the as-spun (10 m/s)  $\text{La}_{0.8-x}\text{Ce}_{0.2}\text{Y}_x\text{MgNi}_{3.5}\text{Co}_{0.4}\text{Al}_{0.1}$  ( $x = 0$  to 0.2) alloys: (a), (b), and (c) are the longitudinal section morphologies of  $\text{Y}_0$ ,  $\text{Y}_{0.1}$ , and  $\text{Y}_{0.2}$  alloys; (d), (e), and (f) are the cross section morphologies of  $\text{Y}_0$ ,  $\text{Y}_{0.1}$ , and  $\text{Y}_{0.2}$  alloys with grain sizes 2.189, 1.633, and 1.094  $\mu\text{m}$ , respectively.

### III. RESULTS AND DISCUSSION

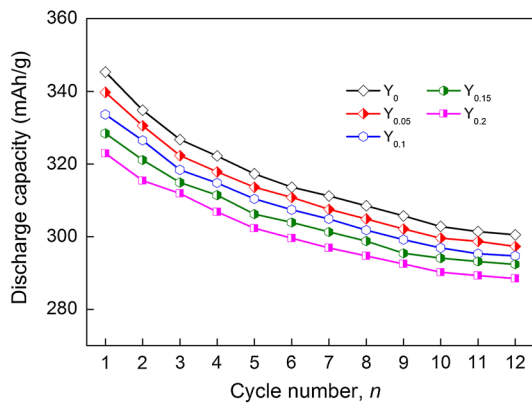
#### A. Structure Characteristics

Figure 1 clearly displays the XRD analysis of the spun and as-cast  $\text{La}_{0.8-x}\text{Ce}_{0.2}\text{Y}_x\text{MgNi}_{3.5}\text{Co}_{0.4}\text{Al}_{0.1}$  ( $x = 0$  to 0.2) alloys. It reveals that the diffraction profiles are similar as well as exhibit sharp peaks, meaning the excellent crystallinities and long-range crystallographic orders of the alloys.<sup>[20]</sup> The ICDD identification demonstrates that these alloys possess multiphase structures containing the major phase  $\text{LaMgNi}_4$  corresponding to  $\text{SnMgCu}_4$  ( $\text{AuBe}_5$ )-type structure with  $F\bar{4}3m$  (216) space group and the minor phase  $\text{LaNi}_5$ . The replacement of Y for La and melt spinning cause a clear transformation of phase abundances without altering phase composition for the alloys. Meanwhile, it is observed that the diffraction peak intensities of the  $\text{LaNi}_5$  phase clearly lower with Y content rising. Figure 2 demonstrates the lattice parameters and phase abundances of  $\text{LaMgNi}_4$  and  $\text{LaNi}_5$  phases, which are evaluated from the XRD data through Jade 6.0. Obviously, the replacement of Y for La makes the lattice parameters and cell volumes of the  $\text{LaMgNi}_4$  and  $\text{LaNi}_5$  phases smaller, which are ascribed to the fact that the radius of La atom is larger than that

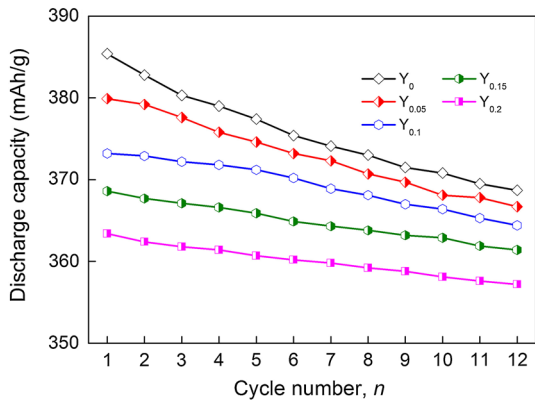
of Y. Moreover, it is found that the replacement of Y for La and melt spinning bring on a rise of  $\text{LaMgNi}_4$  phase content and a decline of  $\text{LaNi}_5$  phase content; however, the mechanism needs further study.

The SEM images of the as-cast  $\text{La}_{0.8-x}\text{Ce}_{0.2}\text{Y}_x\text{MgNi}_{3.5}\text{Co}_{0.4}\text{Al}_{0.1}$  ( $x = 0$  to 0.2) alloys displayed in Figure 3 exhibit a typical dendritic structure. The morphologies of the as-cast alloys display obvious characteristics of peritectic reaction with two different color regions. The EDS patterns identify that the gray region is  $\text{LaMgNi}_4$  phase and the bright area is  $\text{LaNi}_5$  phase, which is demonstrated by the XRD detection.  $\text{LaNi}_5$  phase contains appreciable amount of Co from EDS, because the property of Co element is similar to Ni and the solid solubility of Co is very high in  $\text{LaNi}_5$  phase.

Figure 4 displays the cross section and vertical section SEM morphologies of the as-spun (10 m/s)  $\text{La}_{0.8-x}\text{Ce}_{0.2}\text{Y}_x\text{MgNi}_{3.5}\text{Co}_{0.4}\text{Al}_{0.1}$  ( $x = 0$  to 0.2) alloys. For convenience, the spun flake plane touching the wheel is defined as wheel side, while the other one that parallels to the touch plane is defined as gas side. As shown in Figures 4(a) through (c), the grain sizes and morphologies of the spun flake have clear transformations from the wheel side to the gas side. The farther the distance



(a)



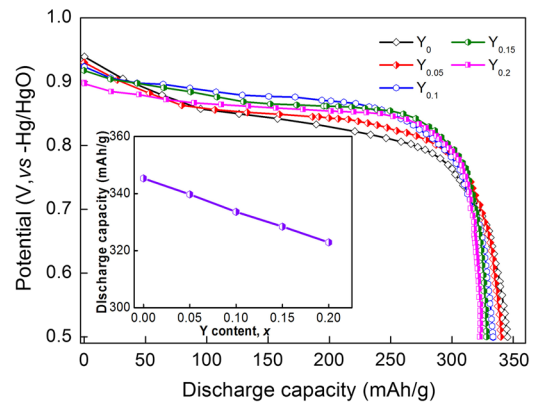
(b)

Fig. 5—Evolution of the discharge capacity of the as-cast and spun  $\text{La}_{0.8-x}\text{Ce}_{0.2}\text{Y}_x\text{MgNi}_{3.5}\text{Co}_{0.4}\text{Al}_{0.1}$  ( $x = 0$  to  $0.2$ ) alloys with cycle number: (a) As-cast, (b) As-spun (10 m/s).

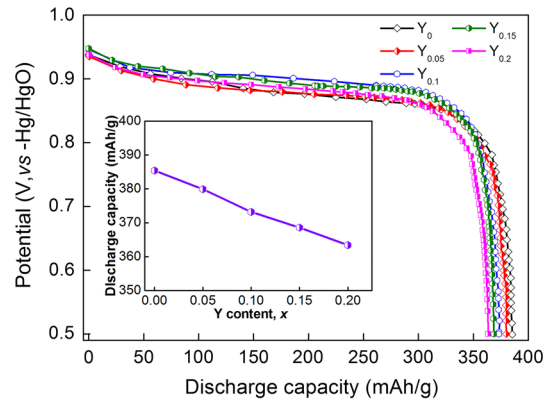
away from wheel side is, the larger the grain size grows. It is very evident that the morphologies of the grains closing to the wheel side are fine isometric crystal, and columnar crystal area is formed at gas side. The vertical section morphologies at about half flake thickness exhibit clear isometric crystal, as shown in Figures 4(d) through (f). Using the line-intercept technique, the grain sizes of  $\text{Y}_0$ ,  $\text{Y}_{0.1}$ , and  $\text{Y}_{0.2}$  alloys are determined to be 2.189, 1.633, and 1.094  $\mu\text{m}$ , respectively. The result indicates that the replacement of Y for La brings on the grains of the alloys obviously refined, meaning that such substitution is advantageous to the nucleation rate but not conducive to the growth rate of no-equilibrium crystallization.

### B. Activation Capability, Potential Characteristic, and Discharge Capacity

Figure 5 displays the activation and discharge capacities of the  $\text{La}_{0.8-x}\text{Ce}_{0.2}\text{Y}_x\text{MgNi}_{3.5}\text{Co}_{0.4}\text{Al}_{0.1}$  ( $x = 0$  to  $0.2$ ) alloys at a low current density of 60 mA/g and only needs testing a dozen times of charge–discharge cycle. It is noted that the alloys reach their maximum discharge capacities just at the initial charging–discharging cycle without the need for any activation, demonstrating that the alloys exhibit excellent activation performance and the replacement of Y for La and melt spinning have no



(a)



(b)

Fig. 6—Discharge potential curves of the as-cast and spun  $\text{La}_{0.8-x}\text{Ce}_{0.2}\text{Y}_x\text{MgNi}_{3.5}\text{Co}_{0.4}\text{Al}_{0.1}$  ( $x = 0$  to  $0.2$ ) alloys: (a) As-cast, (b) As-spun (10 m/s).

influence on the activation ability. In addition, the discharge capacities of the spun samples are all higher than those of the as-cast ones.

Figure 6 presents the discharge potential curves of  $\text{La}_{0.8-x}\text{Ce}_{0.2}\text{Y}_x\text{MgNi}_{3.5}\text{Co}_{0.4}\text{Al}_{0.1}$  ( $x = 0$  to  $0.2$ ) alloys at a current density of 60 mA/g. The discharge potential characteristic is intimately relevant to the cycle stability of the output power of a battery, which is evaluated by the potential plateau of the alloy electrode's discharge curves. The more horizontal and longer the discharge potential plateau is, the better the discharge potential performance of the alloy will be. Obviously, the experimental alloys exhibit good potential characteristics, and the Y substitution for La and melt spinning can visibly ameliorate the discharge potential performances, lengthening discharge plateau and enhancing discharge potential. The variation of discharge capacity with Y content rising is plotted in Figure 6. Evidently, the discharge capacity clearly reduces with the ascending of Y content for these alloys. The discharge capacity reduces from 345.3 to 322.9 mAh/g for the as-cast alloys and from 385.4 to 363.4 mAh/g for the as-spun (10 m/s) alloys when Y content increases from 0 to 0.2. It is noted that the as-spun alloy possesses much higher discharge capacity compared with the as-cast alloy for the same

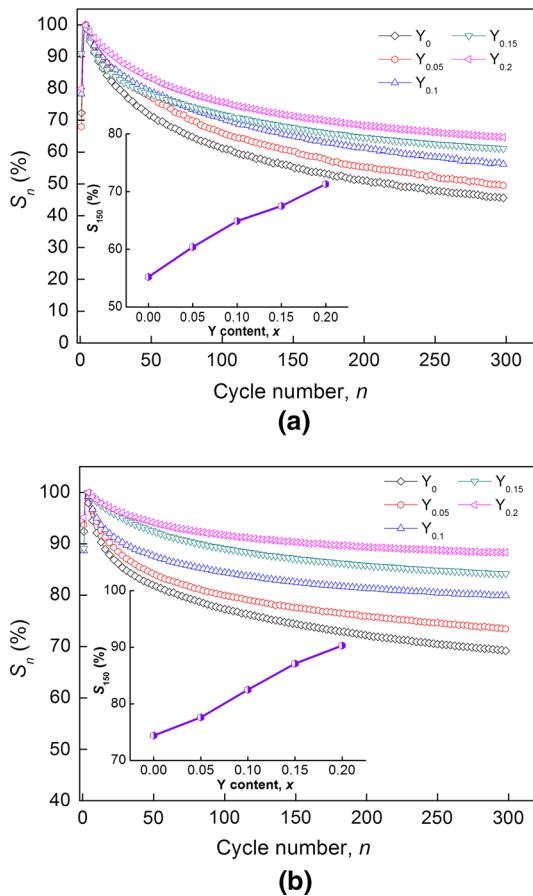


Fig. 7—Evolution of the capacity retaining rates ( $S_n$ ) of the as-cast and spun  $\text{La}_{0.8-x}\text{Ce}_{0.2}\text{Y}_x\text{MgNi}_{3.5}\text{Co}_{0.4}\text{Al}_{0.1}$  ( $x = 0$  to  $0.2$ ) alloys: (a) As-cast, (b) As-spun (10 m/s).

Y content, demonstrating that the melt spinning facilitates the enhancement of the alloy's discharge capacity.

The above research results indicate that the La replacement by Y and melt spinning make obvious effects on the electrochemical characteristics for these alloys, which is deemed to be associated with the structures changed by Y substitution and melt spinning. The outstanding activation performance of the alloys is principally attributed to their multiphase structures owing to the fact that the phase boundary can be viewed as the buffer zone to relieve the strain energy and lattice distortion formed during the process of hydrogen absorption. As for the potential characteristic of an alloy, it is convinced to be directly relevant to the battery's internal resistance, containing ohmic internal resistance and polarization resistance. It is basically determined by the capability of H atoms diffusion and decreases with diffusion coefficient increasing.<sup>[21]</sup> The substitution of La by Y and melt spinning have a positive contribution on the potential characteristic, which is most likely owing to the dramatic refinement of the alloy grains because the grain boundaries can play a role of the fast diffusion path for H atoms.<sup>[22]</sup> Considering the discharge capacity of an alloy, it is deemed to be affected by various factors, including phase

composition, grain size, surface state, composition uniformity, and crystal structure. The decreased discharge capacity of the alloys induced by Y substitution for La is most likely associated with the shrinkage of the cell volume caused by this replacement due to a generally acknowledged fact that the discharge capacity is proportional to the cell volume.<sup>[23]</sup> The favorable effect of melt spinning on the discharge capacity is attributed to the grains refinement caused by melt spinning since the grain boundaries display a distribution of the maximum hydrogen concentrations.<sup>[23]</sup>

### C. Electrochemical Cycle Stability

The electrochemical cycle stability is defined as the ability of alloy electrode resisting capacity degradation and expressed by capacity retaining rate ( $S_n$ ), namely  $S_n = C_n/C_{\text{max}} \times 100$  pct, where  $C_n$  is the discharge capacity of the  $n$ th charge–discharge cycle and  $C_{\text{max}}$  is the maximum value of discharge capacity at a current density of 300 mA/g. The electrochemical cycle stability is one of the important property indicators that determine whether an alloy can be applied in practical negative electrode or not. The activation property is affected by the test current density. Figure 7 is obtained at a traditional current density of 300 mA/g, and the activation process is needed. Figure 7 displays the changes of  $S_n$  values of the  $\text{La}_{0.8-x}\text{Ce}_{0.2}\text{Y}_x\text{MgNi}_{3.5}\text{Co}_{0.4}\text{Al}_{0.1}$  ( $x = 0$  to  $0.2$ ) with cycle number increasing, which clearly exhibits a decline tendency of the discharge capacity. The decline rate of discharge capacity is found to conspicuously decrease with Y content rising, implying that the La replaced by Y plays a positive contribution for the electrochemical cycle stability. To directly prove the impact of Y substitution on the electrochemical cycle stability, the variation of  $S_{150}$  ( $n = 150$ ) values with the increase of Y content is inserted in Figure 7. Notably, the  $S_{150}$  values increase with Y content growing. In particular, the  $S_{150}$  of as-cast alloy is raised from 55.2 to 71.3 pct by adding Y from 0 to 0.2, while that of as-spun (10 m/s) alloy is ascended from 74.4 to 90.3 pct. It is obvious that the as-spun alloy exhibits much larger  $S_n$  value compared with the as-cast alloy for the same Y content, demonstrating that melt spinning plays a significant contribution on the alloy's electrochemical cycle stability.

It has been understood already that the primary reasons for the produce of capacity degradation are pulverization and oxidation for these alloys.<sup>[24,25]</sup> The lattice internal stresses and cell volume change, which are inevitably engendered by H atoms entering the interstitial voids, have been considered to be the reality driving force that causes the alloy's pulverization. To investigate the electrochemical cycle stability mechanism of the alloy electrodes, the morphological change of the alloy particles is observed by SEM before and after electrochemical cycle, as illustrated in Figure 8. Before cycling, the  $Y_0$  alloy particle exhibits a very smooth surface without any crack, whereas many cracks can be seen on the surfaces of the alloy particles after electrochemical cycles, demonstrating that the pulverization of alloy particles appears when the alloy experiences

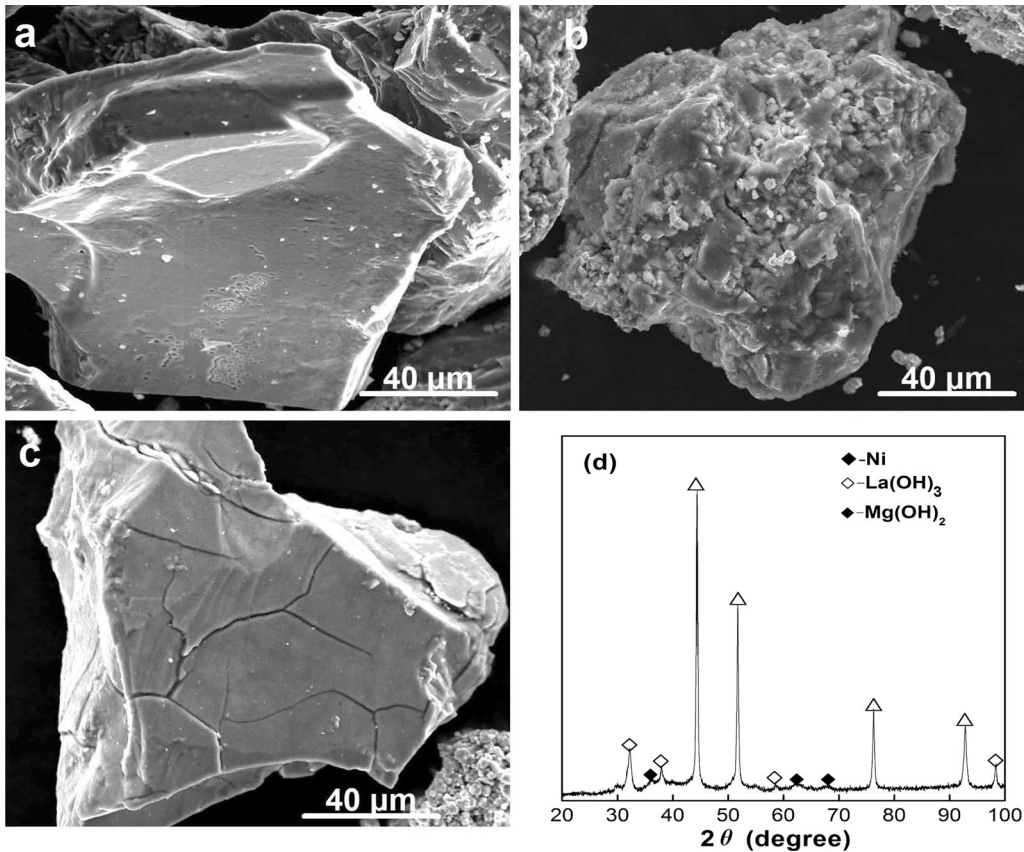


Fig. 8—SEM morphologies together with typical XRD pattern of the as-spun alloys before and after electrochemical cycle: (a) As-spun (10 m/s)  $Y_0$  alloy before cycling; (b) and (c) As-spun (10 m/s)  $Y_0$  and  $Y_{0.2}$  alloys after cycling; (d) XRD of As-spun (10 m/s)  $Y_0$  alloy after cycling.

electrochemical cycles. It is clear that the surface of the  $Y_0$  alloy particles after undergoing cycles is coated by a rough and gossypine layer (Figure 8(b)), which is identified to be  $Mg(OH)_2$  and  $La(OH)_3$  by XRD, as shown in Figure 8(d). It is very interesting that there is much less hydroxide covering the layer appearing on the surface of  $Y_{0.2}$  alloy (see Figure 8(c)), implying that the La substitution by Y can remarkably ameliorate the anti-corrosion and anti-oxidation abilities of the alloys. Moreover, Figures 4(d) through (f) show that the grain sizes of the alloys are obviously reduced by Y substitution. According to these results, it can be concluded that the positive contribution of melt spinning and Y replacement for La to the electrochemical cycle stability is owed to the grain refinement due to a well-known fact that the strength and toughness of an alloy increase with the grain size decreasing. In other words, the smaller the size of alloy grain is, the better its strength and toughness will be, meaning the higher the anti-pulverization capability will be. Moreover, the improved anti-corrosion and anti-oxidation abilities resulting from La substitution by Y is very beneficial to further ameliorate the cycle stability of the alloy.

#### D. Electrochemical Dynamics

The electrochemical dynamic property is characterized by high-rate discharge ability (HRD) for an alloy electrode, which is defined as:  $HRD = C_i/C_{60} \times 100$  pct,

where  $C_i$  and  $C_{60}$  are the maximum values of discharge capacity that charged-discharged at the current densities of  $i$  and 60 mA/g, respectively. Figure 9 presents the variations of the HRD values of the  $La_{0.8-x}Ce_{0.2}Y_xMgNi_{3.5}Co_{0.4}Al_{0.1}$  ( $x = 0$  to 0.2) alloys. The HRD values visibly descend with current density ascending for these alloys. For comparison, the 300 mA/g current density ( $i = 300$  mA/g) is taken as a criterion; thus, the functions of Y content with values of HRD can be determined, which are supplemented in Figure 9. Clearly, the HRD values initially ascend and subsequently descend with Y content increasing for the alloys. The maximum HRD is 92.1 pct for the as-cast alloy and 95.8 pct for the as-spun (10 m/s) alloy, which are obviously superior to the HRD of the RE-based  $AB_5$ -type alloy.<sup>[26]</sup>

To clarify the kinetic mechanism of the experimental alloys, the impacts of Y replacement on the diffusion ability of H atom and charge-transfer rate are studied based on the well-known fact that the HRD is mainly determined by the diffusion ability of H atom in alloy bulk and the charge-transfer rate of H atom on alloy electrode surface.<sup>[27]</sup> The semilogarithmic curves of anodic current varying with operating time prolonging for the alloy electrode are plotted in Figure 10. From the slope of the linear region of the corresponding plots, the diffusion coefficient of H atom can be evaluated based on the following equations<sup>[28]</sup>:

$$\lg i = \lg [\pm 6FD(C_0 - C_s)/(da^2)] - [\pi^2 Dt/3.303a^2], \quad [1]$$

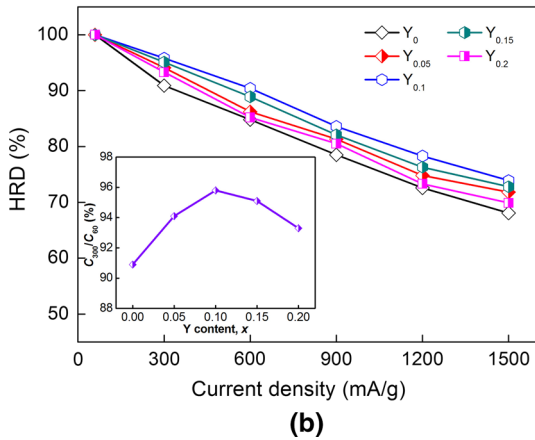
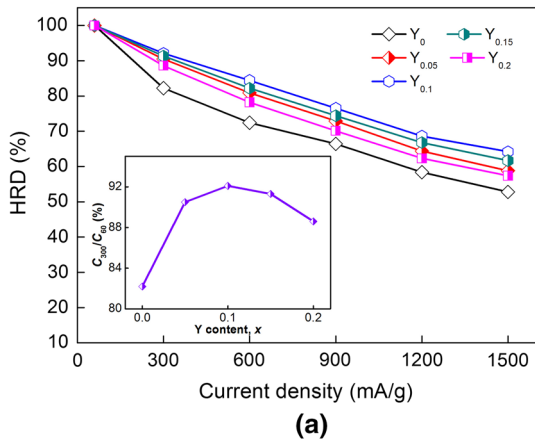


Fig. 9—Evolution of the HRD of the as-cast and spun  $\text{La}_{0.8-x}\text{Ce}_{0.2}\text{Y}_x\text{MgNi}_{3.5}\text{Co}_{0.4}\text{Al}_{0.1}$  ( $x = 0$  to  $0.2$ ) alloys with current density: (a) As-cast, (b) As-spun (10 m/s).

$$D = -2.303a^2[d(\lg i)/d(\lg t)]/\pi^2, \quad [2]$$

where  $i$  is the diffusion current density (A/g), and  $D$  denotes the hydrogen diffusion coefficient ( $\text{cm}^2/\text{s}$ ). The initial hydrogen concentration in the bulk alloy and the hydrogen concentration on the surface of alloy particles are expressed by  $C_0$  and  $C_s$  ( $\text{mol}/\text{cm}^3$ ), respectively.  $d$  is the density of hydrogen storage alloy ( $\text{g}/\text{cm}^3$ ).  $a$  is the radius of alloy particle (cm).  $t$  is the discharge time (0 to 5000 seconds). The  $D$  values calculated from Eq. [2] as a function of Y content are inserted in Figure 10. Obviously, the  $D$  value of the alloy initial ascends and subsequently descends with the increase of Y content. The limiting current density ( $I_L$ ) is another important dynamics property relating to the diffusion ability of H atoms, which can be evaluated from a potentiodynamic polarization curve (*i.e.*,  $I$ - $V$  curves) of alloy electrode, as illustrated in Figure 11. The distinct inflection point appears at each anodic polarization curve and the current value corresponding to inflection point is defined as  $I_L$ , at which an oxidation reaction has happened on the electrode surface, and consequently an oxidation layer is formed and hinders H atoms diffusion.<sup>[14]</sup> Hence,  $I_L$  is regarded to be a critical current density for passivation. Using the data in Figure 11, a function

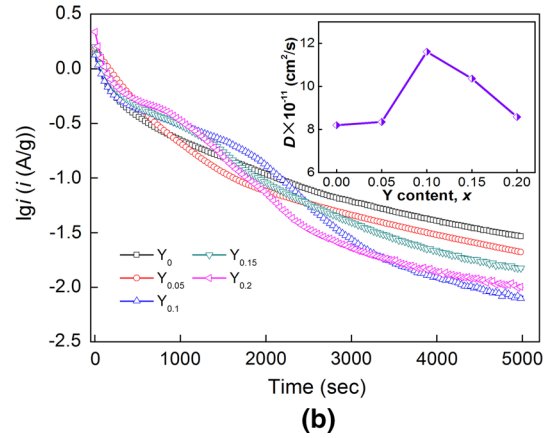
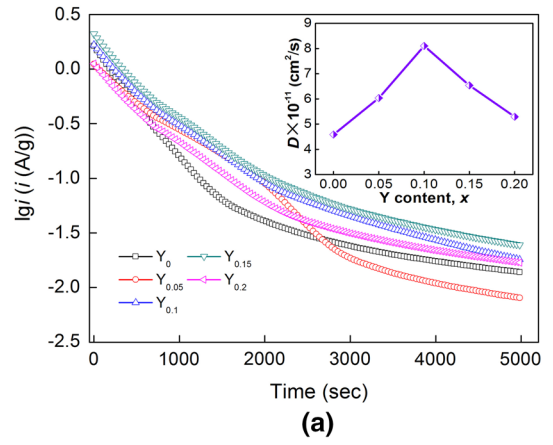


Fig. 10—Semilogarithmic curves of anodic current vs time responses of the as-cast and spun  $\text{La}_{0.8-x}\text{Ce}_{0.2}\text{Y}_x\text{MgNi}_{3.5}\text{Co}_{0.4}\text{Al}_{0.1}$  ( $x = 0$  to  $0.2$ ) alloys: (a) As-cast, (b) As-spun (10 m/s).

of  $I_L$  value with Y addition can be obtained, supplemented in Figures 11(a) and (b). Obviously, these  $I_L$  values initial ascend and subsequently descend with the increase of Y addition. Based on Figures 10 and 11, it can be inferred that the La substitution by Y incurs beneficial and detrimental effects on the diffusion coefficients of H atoms. The grain refined by La substitution by Y evidently brings on an enhancement of the diffusion ability of hydrogen atoms, just as mentioned previously. The negative impact caused by the replacement of Y for La is ascribed to the decrease of cell volume, because a reduction in lattice constants and cell volume will increase the diffusion activation energy of H atoms, consequently impairing H diffusion.<sup>[29]</sup>

Regarding charge-transfer rate on alloy electrode surface, it can be determined from the electrochemical impedance spectrum (EIS) according to the Kuriyama's model.<sup>[30]</sup> As a typical representative, the EIS curves of  $\text{La}_{0.8-x}\text{Ce}_{0.2}\text{Y}_x\text{MgNi}_{3.5}\text{Co}_{0.4}\text{Al}_{0.1}$  ( $x = 0$  to  $0.2$ ) alloys are plotted in Figure 12. There are two separately crooked capacitive loops at middle- and high-frequency areas accompanying a straight line at the low-frequency area in each EIS, which correctly reflects the electrochemical pathway of alloy electrodes. The straight line corresponds to Warburg impedance, and the larger



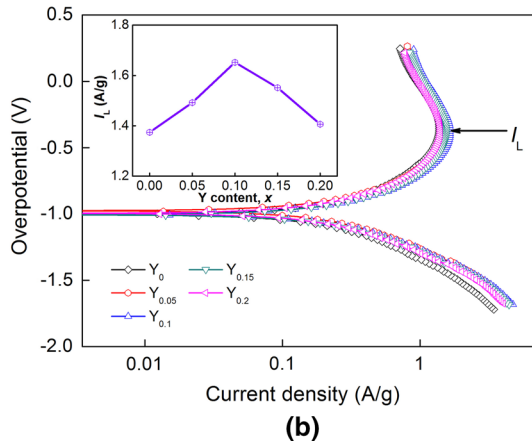
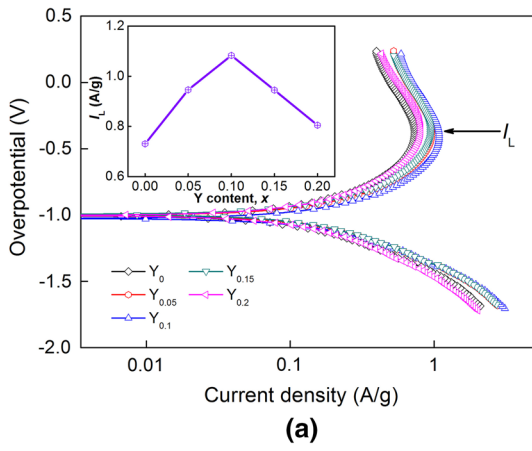


Fig. 11—Potentiodynamic polarization curves of the as-cast and spun  $\text{La}_{0.8-x}\text{Ce}_{0.2}\text{Y}_x\text{MgNi}_{3.5}\text{Co}_{0.4}\text{Al}_{0.1}$  ( $x = 0$  to  $0.2$ ) alloys: (a) As-cast, (b) As-spun (10 m/s).

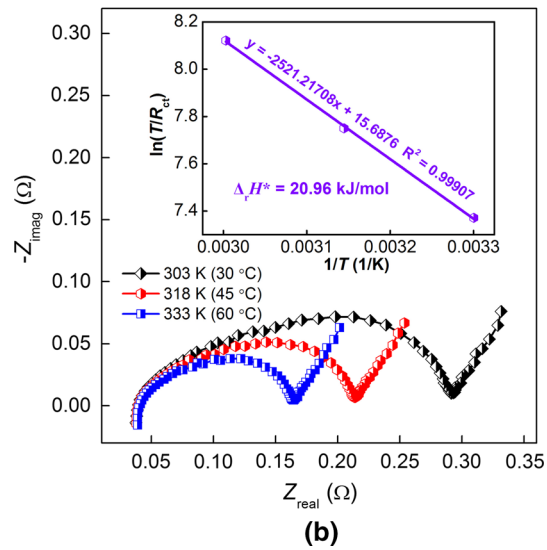
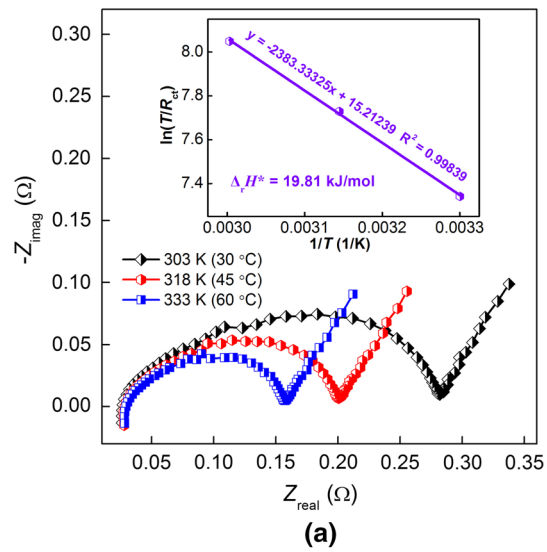


Fig. 13—Electrochemical impedance spectra (EIS) of the as-cast and spun (10 m/s)  $\text{Y}_{0.1}$  alloy at various temperatures: (a) As-cast, (b) As-spun (10 m/s).

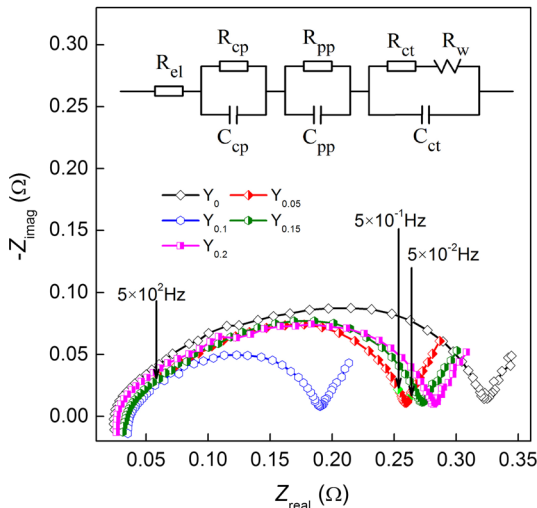


Fig. 12—Electrochemical impedance spectra (EIS) of the as-cast  $\text{La}_{0.8-x}\text{Ce}_{0.2}\text{Y}_x\text{MgNi}_{3.5}\text{Co}_{0.4}\text{Al}_{0.1}$  ( $x = 0$  to  $0.2$ ) alloys and the equivalent circuit.

semicircle at middle-frequency area characterizes the charge-transfer resistance ( $R_{ct}$ ) on alloy electrode surface. By means of the equivalent circuit, as inserted in

Figure 12, the  $R_{ct}$  values can be obtained using the fitting program Z-View. As considered by Kuriyama *et al.*, the  $R_{ct}$  value basically depends on both the reactivity of the alloy electrode surface and reaction area. The electrochemical reactivity of the alloy electrode surface can be determined with apparent activation enthalpy  $\Delta_r H^*$ , which can be obtained by the following equation<sup>[30,31]</sup>:

$$\ln[(T/R_{ct})/(K/\Omega)] = C_0 - \Delta_r H^*/(RT), \quad [3]$$

where  $R$  is the gas constant,  $T$  is the temperature of sample,  $K$  is the unit of temperature,  $\Omega$  is the unit of resistance, and  $C_0$  is a constant in which the surface area is included. Considering the calculation conditions of Eq. [3], the EIS curves of  $\text{La}_{0.8-x}\text{Ce}_{0.2}\text{Y}_x\text{MgNi}_{3.5}\text{Co}_{0.4}\text{Al}_{0.1}$  ( $x = 0$  to  $0.2$ ) alloys are measured at different temperatures [303 K, 318 K, and 333 K (30 °C, 45 °C, and 60 °C)]; as a representative, the EIS curves of the

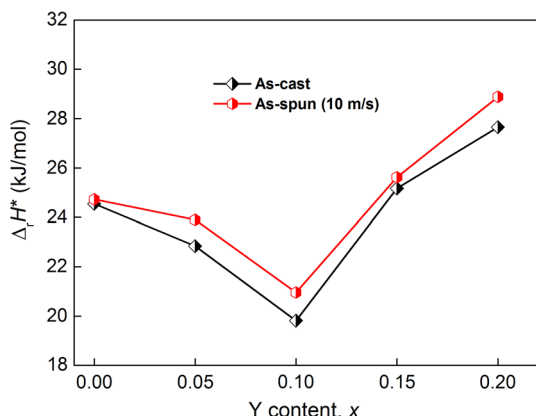


Fig. 14—Evolution of the activation enthalpy  $\Delta_r H^*$  values of the as-cast and spun (10 m/s)  $\text{La}_{0.8-x}\text{Ce}_{0.2}\text{Y}_x\text{MgNi}_{3.5}\text{Co}_{0.4}\text{Al}_{0.1}$  ( $x = 0$  to 0.2) alloys with Y content.

as-cast and spun (10 m/s)  $\text{Y}_{0.1}$  alloy are shown in Figure 13. Utilizing the data in Figure 13, the Kuriyama graphs of  $\ln(T/R_{ct})$  vs  $1/T$  can be plotted using logarithmic transformation of Eq. [3], as illustrated in Figure 13. From the slopes of Kuriyama plots,  $\Delta_r H^*$  values can be calculated easily. Thereby, the variations of  $\Delta_r H^*$  value with Y content growing are obtained, as supported in Figure 14. The  $\Delta_r H^*$  values of the alloys initial decrease and subsequently increase with Y content growing, namely existing an optimal amount of Y substitution that the alloys possess the largest charge-transfer rate. It indicates that the Y replacement for La in the alloys causes a positive and negative influence on the charge-transfer rate. The positive contribution is considered to be the aspect of the enhanced corrosion resistance which can suppress further oxidation of La and Mg as well as induce the formation of a Ni enrichment layer,<sup>[32]</sup> hence leading to an improvement of the electrocatalytic activity on alloy electrode surface. The negative impact is most likely the aspect in grain refinement because the refined grains facilitate the prevention of pulverization of alloy electrode during charge–discharge cycles,<sup>[33]</sup> reduce functional new surface on electrode, as well as lessen charge-transfer rate at the interface between the electrode and electrolyte.

#### IV. CONCLUSIONS

A systematical investigation on the microstructures and electrochemical hydrogen storage characteristics of  $\text{La}_{0.8-x}\text{Ce}_{0.2}\text{Y}_x\text{MgNi}_{3.5}\text{Co}_{0.4}\text{Al}_{0.1}$  ( $x = 0$  to 0.2) alloys has been conducted and the major conclusions are summarized as follows:

1. The structure characterization of  $\text{La}_{0.8-x}\text{Ce}_{0.2}\text{Y}_x\text{MgNi}_{3.5}\text{Co}_{0.4}\text{Al}_{0.1}$  ( $x = 0$  to 0.2) alloys shows that the Y substitution for La brings on an increase in the  $\text{LaMgNi}_4$  phase content and a decrease in the amount of  $\text{LaNi}_5$  phase while

maintaining the phase compositions of the alloys. Moreover, this substitution leads the alloy grains to be refined significantly.

2. The electrochemical tests show that the alloys exhibit super activation capability. The replacement of Y for La significantly improves the discharge potential characteristics of the alloys, but it causes an undesired decline in discharge capacity of the alloys. However, this substitution dramatically ameliorates cycle stability.
3. The electrochemical dynamics of alloys, including HRD, diffusion coefficient ( $D$ ), limiting current density ( $I_L$ ), and charge-transfer rate, initially increase and subsequently decrease with the increasing Y content, for which the modified structure induced by Y substitution for La is principally responsible. The hydrogen diffusion coefficient ( $D$ ) and the activation enthalpy ( $\Delta_r H^*$ ) are thought to be the main controlling factors of the high-rate discharge abilities (HRDs) of the alloys.

#### ACKNOWLEDGMENTS

This work was financially supported by the National Natural Science Foundation of China (51371094 and 51471054) and the Natural Science Foundation of Inner Mongolia, China (2015MS0558).

#### REFERENCES

1. D. Mori and K. Hirose: *Int. J. Hydrog. Energy*, 2009, vol. 34, pp. 4569–74.
2. R. Lan, J.T.S. Irvine, and S. Tao: *Int. J. Hydrog. Energy*, 2012, vol. 37, pp. 1482–94.
3. I.P. Jain, C. Lal, and A. Jain: *Int. J. Hydrog. Energy*, 2010, vol. 35, pp. 5133–44.
4. R.F. Li, P.Z. Xu, Y.M. Zhao, J. Wan, X.F. Liu, and R.H. Yu: *J. Power Sources*, 2014, vol. 270, pp. 21–27.
5. L.Z. Ouyang, Z.J. Cao, L.L. Li, H. Wang, J.W. Liu, D. Min, Y.W. Chen, F.M. Xiao, R.H. Tang, and M. Zhu: *Int. J. Hydrog. Energy*, 2014, vol. 39, pp. 12765–72.
6. K. Kadir, D. Noreus, and I. Yamashita: *J. Alloys Compd.*, 2002, vol. 345, pp. 140–43.
7. T. Kohno, H. Yoshida, F. Kawashma, T. Inaba, I. Sakai, M. Yamamoto, and M. Kanda: *J. Alloys Compd.*, 2000, vol. 311, pp. L5–L7.
8. Z.M. Wang, H.Y. Zhou, Z.F. Gu, G. Cheng, and A.B. Yu: *J. Alloys Compd.*, 2004, vol. 377, pp. L7–L9.
9. Y.F. Liu, H.G. Pan, M.X. Gao, and Q.D. Wang: *J. Mater. Chem.*, 2011, vol. 21, pp. 4743–55.
10. Y.F. Liu, Y.H. Cao, L. Huang, M.X. Gao, and H.G. Pan: *J. Alloys Compd.*, 2011, vol. 509, pp. 675–86.
11. A. Teresiak, M. Uhlemann, J. Thomas, J. Eckert, and A. Gebert: *J. Alloys Compd.*, 2014, vol. 582, pp. 647–58.
12. X. Tian, G.H. Yun, H.Y. Wang, T. Shang, Z.Q. Yao, W. Wei, and X.X. Liang: *Int. J. Hydrog. Energy*, 2014, vol. 39, pp. 8474–81.
13. T. Yang, T.T. Zhai, Z.M. Yuan, W.G. Bu, S. Xu, and Y.H. Zhang: *J. Alloys Compd.*, 2014, vol. 617, pp. 29–33.
14. T.T. Zhai, T. Yang, Z.M. Yuan, and Y.H. Zhang: *Int. J. Hydrog. Energy*, 2014, vol. 39, pp. 14282–87.
15. T. Yang, Z.M. Yuan, W.G. Bu, Z.C. Jia, Y. Qi, and Y.H. Zhang: *Mater. Design*, 2016, vol. 93, pp. 46–52.
16. Y.H. Zhang, Y. Cai, C. Zhao, T.T. Zhai, G.F. Zhang, and D.L. Zhao: *Int. J. Hydrog. Energy*, 2012, vol. 37, pp. 14590–97.

17. Y.H. Zhang, B.W. Li, H.P. Ren, Z.W. Wu, X.P. Dong, and X.L. Wang: *J. Alloys Compd.*, 2008, vol. 461, pp. 591–97.
18. A. Teresiak, A. Gebert, M. Savyak, M. Uhlemann, C. Mickel, and N. Mattern: *J. Alloys Compd.*, 2005, vol. 398, pp. 156–64.
19. Y.H. Zhang, T.T. Zhai, T. Yang, Z.M. Yuan, Z.H. Hou, and Y. Qi: *J. Appl. Electrochem.*, 2015, vol. 45, pp. 931–41.
20. A. Züttel: *Mater. Today*, 2003, vol. 6, pp. 24–33.
21. W.H. Lai and C.Z. Yu: *Battery Bimon.*, 1996, vol. 26, pp. 189–91.
22. Y. Wu, W. Hana, S.X. Zhou, M.V. Lototsky, J.K. Solberg, and V.A. Yartys: *J. Alloys Compd.*, 2008, vol. 466, pp. 176–81.
23. S. Orimo and H. Fujii: *Appl. Phys. A*, 2001, vol. 72, pp. 167–86.
24. Y.F. Liu, H.G. Pan, M.X. Gao, Y.Q. Lei, and Q.D. Wang: *J. Alloys Compd.*, 2005, vol. 403, pp. 296–304.
25. D. Chartouni, F. Meli, A. Züttel, K. Gross, and L. Schlapbach: *J. Alloys Compd.*, 1996, vol. 241, pp. 160–66.
26. Y.F. Liu, H.G. Pan, Y.F. Zhu, R. Li, and Y.Q. Lei: *Mater. Sci. Eng. A*, 2004, vol. 372, pp. 163–72.
27. X.Y. Zhao, Y. Ding, L.Q. Ma, L.Y. Wang, M. Yang, and X.D. Shen: *Int. J. Hydrog. Energy*, 2008, vol. 33, pp. 6727–33.
28. G. Zhang, B.N. Popov, and R.E. White: *J. Electrochem. Soc.*, 1995, vol. 142, pp. 2695–98.
29. N. Cui and J.L. Luo: *Int. J. Hydrog. Energy*, 1999, vol. 24, pp. 37–42.
30. N. Kuriyama, T. Sakai, H. Miyamura, I. Uehara, H. Ishikawa, and T. Iwasaki: *J. Alloys Compd.*, 1993, vol. 202, pp. 183–97.
31. H.L. Ding, S.M. Han, Y. Liu, J.S. Hao, Y. Li, and J.W. Zhang: *Int. J. Hydrog. Energy*, 2009, vol. 34, pp. 9402–08.
32. S. Ruggeri, L. Roué, J. Huot, R. Schulz, L. Aymard, and J.M. Tarascon: *J. Power Sources*, 2002, vol. 112, pp. 547–56.
33. Y.H. Zhang, B.W. Li, H.P. Ren, Y. Cai, X.P. Dong, and X.L. Wang: *J. Alloys Compd.*, 2008, vol. 458, pp. 340–45.